https://doi.org/10.5194/egusphere-2026-2930
Preprint. Discussion started: 1 June 2026

Toward shellfish aquaculture circularity: stimulating mussel shell dissolution in marine sediments

Cedric Goossens[1], Steven Bouillon[2], Filip J. R. Meysman[1], Sebastiaan J. van de Velde[3,4]

[1]Geobiology Research Group, University of Antwerp, Wilrijk, 2610, Belgium
[2]Division of Soil and Water Management, Katholieke Universiteit Leuven, Heverlee, 3001, Belgium
[3]Department of Marine Science, University of Otago, Ōtepoti Dunedin, 9016, Aotearoa New Zealand
[4]Earth Sciences New Zealand, Te Whanganui-a-Tara Wellington, 6021, Aotearoa New Zealand

Correspondence to: Cedric Goossens (Cedric.Goossens@uantwerpen.be)

Abstract. Ocean alkalinity enhancement (OAE) is receiving considerable attention as a carbon dioxide (CO_2) removal strategy, and novel approaches to increase the total alkalinity (A_T) of the surface ocean are being explored. In bivalve aquaculture, calcification during shell growth consumes A_T, thus leading to CO_2 emissions. After consumption, shells are typically landfilled or incinerated, which can generate additional CO_2 emissions. Here, we investigate whether bivalve shells could be a potential resource for mineral-based OAE. The idea is to grind the calcium carbonate ($CaCO_3$) shells to increase the reactive surface area and distribute them into permeable, oxygen-rich sediments, where their dissolution produces A_T that could then compensate the CO_2 emitted during calcification. To evaluate this concept, we conducted microcosm incubations of sediments amended with crushed mussel shells (~8 wt%), and monitored the sediment geochemistry and sediment-water exchange over 24 weeks. Control sediments exhibited low and constant $CaCO_3$ dissolution rates (R_{diss} = 0.9 ± 0.5 mmol m^{-2} d^{-1}) and A_T fluxes (F_{AT} = 3.2 ± 1.1 mmol m^{-2} d^{-1}). In contrast, shell-amended sediments showed markedly higher R_{diss} and F_{AT} values, which exhibited a transient response modulated by oxygen and organic matter availability. Initially, shell dissolution was restricted by oxygen availability due to the intense mineralization of shell-associated organic matter. Subsequently, following gradual sediment reoxygenation, dissolution rates increased, reaching a maximum R_{diss} of 22.7 ± 2.6 mmol m^{-2} d^{-1} after 9 weeks, corresponding to a measured F_{AT} of 43.0 ± 6.0 mmol m^{-2} d^{-1}. After that, $CaCO_3$ dissolution rates declined as organic matter availability decreased, thus reducing dissolution toward a constant steady-state R_{diss} of 2.2 ± 1.1 mmol m^{-2} d^{-1}. After 6 months, ~6 % of the initial shell mass had dissolved, and extrapolation of the new quasi-steady-state dissolution rate at the end of the experiment suggests that complete dissolution would take ~38 years. Our results suggest that organic matter availability limits $CaCO_3$ dissolution in the permeable sediment investigated. This constraint, however, can be alleviated by targeting environments with high organic matter deposition for in-situ applications, such as sediments beneath mussel farms, thereby promoting mussel aquaculture circularity.

https://doi.org/10.5194/egusphere-2026-2930
Preprint. Discussion started: 1 June 2026

1 Introduction

Climate stabilization requires direct carbon dioxide removal (CDR) from the atmosphere alongside conventional mitigation strategies that prevent new emissions (Gasser et al., 2015; IPCC, 2023; Sanderson et al., 2016). As a consequence, CDR research has gained considerable traction over the last few years (Lück et al., 2025; Minx et al., 2024). Marine CDR options are receiving increased attention due to the large CO_2 buffering capacity of the ocean, which has taken up about 26 % of the global anthropogenic emissions since 1850 (Friedlingstein et al., 2025). The amount of CO_2 that can be stored in the ocean is largely controlled by total alkalinity (A_T), which is a measure of the excess of proton acceptors (bases) over proton donors (acids) in solution (Dickson, 1981; Zeebe & Wolf-Gladrow, 2001). An increase in A_T causes the carbonate system to react by dissociating dissolved CO_2 to bicarbonate (HCO_3^-) and carbonate (CO_3^{2-}), resulting in an increased uptake of atmospheric CO_2. Ocean alkalinity enhancement (OAE) represents one of the proposed marine CDR methods, and aims to establish higher oceanic CO_2 uptake by artificially increasing ocean A_T levels (Oschlies et al., 2023; Renforth & Henderson, 2017).

In recent years, a number of OAE approaches have been investigated in which minerals (silicates and carbonates) are added to coastal sediments (Fuhr et al., 2022, 2023, 2024). These minerals subsequently undergo a slow weathering process, which releases A_T. Up until now, most attention has gone toward purposely mined minerals, such as the silicate mineral olivine (e.g., Flipkens et al., 2023; Geerts et al., 2025). Yet, mining operations require energy, generate environmental impacts, and are challenging to rapidly scale, as new mining sites require long permitting trajectories. Therefore, an alternative option is to consider whether minerals sourced from side and waste streams from existing industrial activities can be used for OAE (Bullock et al., 2021). One such activity is bivalve aquaculture. During shell formation, bivalves remove dissolved inorganic carbon (DIC) from the water to form calcium carbonate ($CaCO_3$). Yet, like any form of carbonate formation, this process also removes alkalinity, as the precipitation of 1 mol of $CaCO_3$ consumes 2 mol of A_T and 1 mol of DIC:

$$Ca^{2+} + 2HCO_3^- \leftrightarrow CaCO_3 + CO_2 + H_2O \quad (1)$$

Overall, carbonate formation results in an increase in the partial pressure of CO_2 (pCO_2) in seawater (Fig. 1a; Frankignoulle et al., 1994, 1995). In shallow coastal environments, where bivalve aquaculture typically takes place, rapid equilibration of the elevated pCO_2 with the atmosphere will result in outgassing of most of the CO_2 produced during $CaCO_3$ formation. As such, bivalve production induces a release of CO_2 into the atmosphere (Pernet et al., 2025).

https://doi.org/10.5194/egusphere-2026-2930
Preprint. Discussion started: 1 June 2026

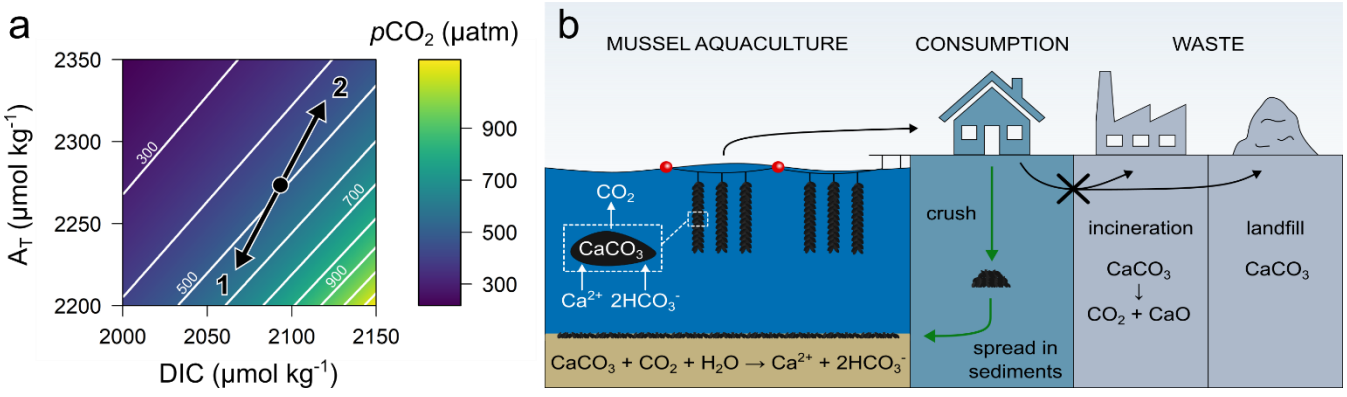

Figure 1. (a) Thermodynamic equilibrium plot of alkalinity (A_T) as a function of dissolved inorganic carbon (DIC) superimposed on contours of partial pressure of CO_2 (pCO_2) at 15 °C and a salinity of 35. Black dot: initial seawater concentration. Calcification (vector 1) reduces A_T and DIC in a 2:1 ratio, which increases pCO_2 and leads to CO_2 degassing to the atmosphere. Carbonate dissolution (vector 2) increases A_T and DIC in a 2:1 ratio, which decreases pCO_2 and leads to CO_2 uptake from the atmosphere. (b) Conceptual scheme illustrating the life cycle of bivalve shells from aquaculture (using mussels as example). Bivalves remove alkalinity (A_T) and dissolved inorganic carbon (DIC) from seawater to form calcium carbonate shells ($CaCO_3$), a process that releases CO_2. After harvest and consumption, shell waste is typically incinerated (with associated CO_2 emission and landfill of CaO-containing ashes) or directly landfilled. The green arrows depict the circular route investigated here. Crushed shells are spread onto shallow sediments, where $CaCO_3$ dissolution generates A_T and leads to atmospheric CO_2 uptake. The overall process offsets the CO_2 released during shell growth.

With a current global production of over 17 million tons of bivalves per year (FAO, 2024, 2025), bivalve aquaculture thus generates considerable CO_2 emissions associated with calcification (~4 million tons of CO_2 yr^{-1}). Life cycle assessments (LCAs) of bivalve aquaculture typically do not account for CO_2 emissions from calcification (see Ray et al., 2018 and references therein), thus resulting in an underestimation of its climate impact. When taken into account, calcification may account for up to 90 % of the total emissions (Ray et al., 2018; Thrane, 2004). Moreover, shell waste is typically either landfilled or incinerated as general waste after consumption. The latter can lead to additional CO_2 emissions, as calcium carbonate undergoes thermal decomposition to produce calcium oxide (CaO, or quicklime) and CO_2 when heated to higher temperature (Fig. 1b):

$$CaCO_3 \rightarrow CO_2 + CaO \quad (2)$$

When the resulting incineration ashes are deposited at a landfill site, some of CaO may react again with CO_2 to form $CaCO_3$, but the degree to which this happens remains uncertain, and will be strongly dependent on landfill conditions.

In this study, we explore an alternative destination for the $CaCO_3$-containing shells after consumption. The core idea is to offset CO_2 emissions associated with calcification (i.e., the reverse of Eq. 1) by reintroducing mussel shells into the marine environment and stimulating shell dissolution (Fig. 1b). The key question is whether the mussel shells will effectively dissolve, and if so, under which conditions and over which timeframes. The precipitation and dissolution of $CaCO_3$ are controlled by the $CaCO_3$ saturation state of seawater (Zeebe & Wolf-Gladrow, 2001) and the reactive surface area of the $CaCO_3$ minerals. Since surface waters are typically oversaturated with respect to $CaCO_3$, dissolution generally does not occur in the water

https://doi.org/10.5194/egusphere-2026-2930
Preprint. Discussion started: 1 June 2026

column (Kleypas, 2011; Morse & Mackenzie, 1990). However, $CaCO_3$ dissolution is possible in the pore water of marine sediments under specific conditions, in a process referred to as metabolic carbonate dissolution, in which CO_2 generated by aerobic mineralization of organic matter builds up in the pore water until undersaturation is achieved and $CaCO_3$ starts to dissolve (Archer et al., 1989; Emerson & Bender, 1981; Lunstrum & Berelson, 2022; Morse et al., 1985; Subhas et al., 2022):

$$CaCO_3 + CH_2O + O_2 \rightarrow Ca^{2+} + 2HCO_3^- \quad (3)$$

The above reaction equation also succinctly summarizes the conditions that promote metabolic $CaCO_3$ dissolution: (1) permeable sediments that enable deep oxygen penetration; (2) sediments sufficiently rich in organic matter, which drives metabolic dissolution; and (3) low ambient $CaCO_3$ concentration, thereby limiting buffering from background $CaCO_3$ (Goossens et al., 2026). Dissolution efficiency could further be improved by grinding shells to a finer size to increase their reactive surface area and enhance their intrinsic dissolution rate. Likewise, the sediments should be located within shallow waters with a well-mixed water column as to allow rapid CO_2 equilibration with the atmosphere.

Here, we assessed the potential for enhanced sedimentary dissolution of $CaCO_3$ shells as a means to compensate for calcification-associated CO_2 emissions. To this end, we selected the blue mussel (*Mytulis edulis*) as the target species, which dominates shellfish aquaculture in Belgium and the Netherlands (FAO, 2025). Previous studies on biogenic shell dissolution (see Gazeau et al., 2013 for an overview) have considered a range of taxa, including oysters (Waldbusser et al., 2011; Welladsen et al., 2010), clams (Green et al., 2004, 2009; McClintock et al., 2009), limpets (McClintock et al., 2009), and snails (Nienhuis et al., 2010), but only a limited number focused on sedimentary environments (Green et al., 2004, 2009). Furthermore, relatively little attention has been given to mussel shells, with the few studies that do address their dissolution primarily focusing on ocean acidification experiments using chemically altered (sea)water conditions (Carlson et al., 2025; Cubillas et al., 2005; Ericson & Ragg, 2022; Gazeau et al., 2007; Melzner et al., 2011). Here, we address this gap by performing laboratory flux incubations with permeable, $CaCO_3$-poor coastal sediments amended with crushed blue mussel shells.

2 Materials and Methods

2.1 Sediment collection and incubation setup

Sediment was collected from a shallow site in the southern North Sea along the Belgian coast (station "Bruggen en Wegen Oostende", 51.28300° N 2.92133° E; Fig. 2a) on the 20th of March 2023. The location is a dredge deposit site characterized by permeable sediment. Sediment was collected using a Van Veen grab sampler, transported to the laboratory, homogenized and stored in the dark at stable room temperature (18-22 °C) with 20 cm of overlying seawater until further use. Air pumps were installed to keep the overlying seawater oxygenated. A subsample of sediment was taken for analysis of grain size distribution and porosity. Natural seawater was used as overlying water in the sediment incubations. This seawater was collected from the Eastern Scheldt (The Netherlands) and filtered through a sand filter (0.5 mm) to remove macrofauna. Blue mussels (*Mytilus edulis*) were sourced from the supermarket and originated from a hanging culture at the Westdiep Sea Farm,

https://doi.org/10.5194/egusphere-2026-2930
Preprint. Discussion started: 1 June 2026

a mussel farming site ~5 km off the Belgian coast at 15 m water depth in the southern North Sea (51.16975° N 2.63104° E; Fig. 2a). Mussel tissue was manually removed, shells were rinsed with fresh water and dried overnight in a drying oven at 60 °C. Dried shells were ground with an ultra-centrifugal mill (ZM 200, Retsch) and the fraction that passed a 0.25 mm sieve was retained. Ground shell samples were collected for analysis of organic and inorganic carbon concentration.

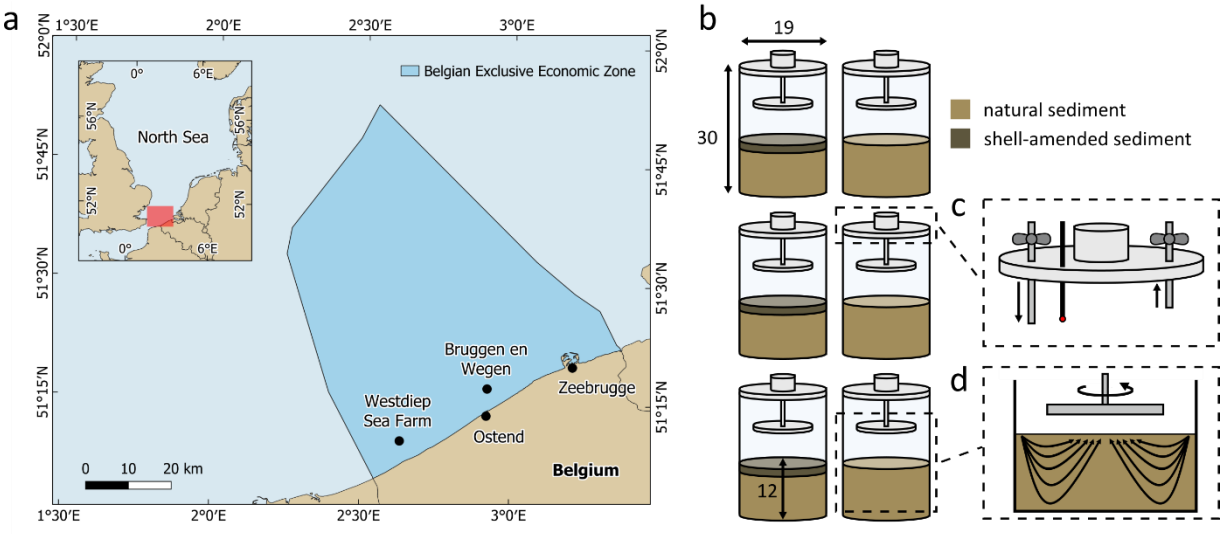

Figure 2: (a) Map of the Belgian part of the North Sea (BPNS), showing the sediment collection site (Bruggen en Wegen) and the mussel farming site (Westdiep Sea Farm). An overview map of the North Sea is provided with the location of the BPNS in red. (b) Experimental setup, consisting of 3 control chambers and 3 treatment chambers amended with crushed mussel shells. Chamber and sediment dimensions are displayed in cm. (c) Chamber top lids contained 3 sampling ports: one was used for an oxygen probe, and the other two for subsampling of the overlying water. Arrows indicate water flow during subsampling: subsamples were taken from one port, while replacement water was added through the other port. (d) Stirring disk rotation induced pore-water exchange through a radial pressure gradient. Arrows indicate pore-water flow through the sediment column.

The sediment microcosms were adapted for the closed incubation of permeable sediments following a well-known flux chamber design (Huettel & Gust, 1992). The flux chambers consisted of polymethyl methacrylate (PMMA) core barrels (19 cm inner diameter, 30 cm height) fitted with a top and bottom lid (Fig. 2b-c). Top lids were equipped with a stirring disk (14 cm diameter), which mixes the overlying seawater and also creates a radial pressure gradient that drives advective pore-water exchange in the permeable sediment (Fig. 2d; Huettel & Gust, 1992). Three sampling ports were installed in the top lids (Fig. 2c): one was used for a fiber-optical oxygen probe (FireSting OXROB10, PyroScience), and the other two for subsampling of the overlying seawater during the incubation.

The experimental setup consisted of 6 flux chambers: 3 replicate control chambers were filled solely with natural sediment (~13 cm), while 3 replicate treatment chambers were filled with a base layer of natural sediment (~11 cm) and a top layer of natural sediment (~2 cm) mixed with 100 g of ground shells, to achieve a concentration of ~8 wt% of added shell material in the mixed top layer. Solid-phase samples for the analysis of total, organic, and inorganic carbon (and its stable isotope composition, i.e. $\delta^{13}C$ values) were collected from the surface sediment in the control and treatment chambers.

https://doi.org/10.5194/egusphere-2026-2930
Preprint. Discussion started: 1 June 2026

Oxygenated filtered seawater was added to the chambers at the start of the incubation. Top lids were installed and chambers were placed in a closed container filled with water to ensure a dark and stable environment.

2.2 Solute flux incubation

Consecutive flux sessions were performed to quantify the uptake or release of solutes across the sediment-water interface by monitoring their accumulation in the overlying water. A total of 11 flux incubation sessions were conducted over the course of 24 weeks (each flux session lasted ~10 days). Before each flux session, the overlying water in the flux chamber was replaced in order to start a new monitoring period of solute accumulation. Each flux session consisted of two parts: a short "closed" part and a longer "open" part, as further detailed below. Throughout the session, the rotating disks were set at 80 rounds per minute (RPM) to stimulate advective pore-water exchange with the overlying water while not disturbing the sediment (i.e., no resuspension). The total time of a single incubation was adjusted to prevent excessive solute concentration build-up (i.e., to avoid saturation effects and secondary mineral precipitation). Before each session, oxygen optodes were calibrated using a two-point calibration with seawater at 0 % (saturated with Na_2SO_3) and 100 % (bubbled with air pumps) O_2 saturation.

In the first "closed" part of the incubation session, atmospheric exchange was prevented by closing the gas-tight top lids. The aim was to obtain O_2 and DIC fluxes, which necessitate isolation from the atmosphere. Closed incubations lasted until the O_2 saturation had dropped from ~100 % at the start to ~60 % to prevent excessive disturbance of the balance between aerobic and anaerobic processes in the sediment (which may influence $CaCO_3$ dissolution). Water samples (25 mL) were taken from one sampling port, while simultaneously replacing the sampled volume with stock seawater through the other port (Fig. 2c). Sampling was done at variable time intervals (5 timepoints) based on the O_2 consumption rates, which were continuously monitored at one-second intervals with the optode. Samples for dissolved inorganic carbon (DIC, 12 mL) and the stable isotope composition of DIC (δ^{13}C-DIC, 6 mL) were filtered (Acrodisc Syringe Filter, 0.8/0.2 µm) and collected in glass exetainers, poisoned with 10 µL $HgCl_2$, and stored upside down in the dark at 4°C.

After the closed incubation, chambers were opened and allowed to reoxygenate, and salinity was measured in the overlying water. In the subsequent "open" incubation, atmospheric exchange was enabled by opening the top lids and placing small bars between the chambers and the lids to keep the overlying water oxygenated. Water samples (60 mL) were taken directly from the overlying water at fixed time intervals (~24 hours in between) with 5-6 time points in total. At every time point, salinity was measured in the overlying water (as to track potential evaporation). Samples for A_T (50 mL) and nutrients (9 mL; NO_3^- and NH_4^+) were filtered through a dual-layer filter (Acrodisc Syringe Filter, 0.8/0.2 µm), collected in plastic vials, and stored unpoisoned in the dark at 4°C and -20°C, respectively.

2.3 Pore-water sampling

At the end of the final flux session, 2 small core liners were inserted into the sediment and recovered for pore-water analysis. Cores were sectioned in an anaerobic glove box at 0.5 cm intervals for the 0-2 cm depth range, 1 cm intervals for the

https://doi.org/10.5194/egusphere-2026-2930
Preprint. Discussion started: 1 June 2026

2-6 cm depth range, and 2 cm intervals for the remaining depth. Pore water was extracted from sediment slices using rhizon samplers. Pore-water samples from one core liner were collected for ICP-OES analysis (Ca^{2+}; 0.5 mL), stored in plastic tubes, diluted 10 times with 0.7M HNO_3, and stored in the dark at 4°C. Pore-water samples from the second core liner were collected for DIC and $\delta^{13}C$-DIC (only samples ≥1 mL were retained), poisoned with 10 µL $HgCl_2$, and stored upside down in exetainers in the dark at 4°C.

2.4 Analytical methods

Grain size distribution was determined using a laser diffraction particle size analyzer (Malvern 2000, Malvern Panalytical) with a precision of <3 % relative standard deviation (RSD) for D_{50}, and <5 % for D_{10} and D_{90}. Porosity was derived from weight loss after freeze-drying, accounting for salt content in the pore water, which was assumed to be equal to the salt content in the overlying water.

Solid-phase samples were analyzed for total carbon and organic carbon content as well as $\delta^{13}C$ values through combustion using an elemental analyzer (EA 1110, CE Instruments), connected via a Conflo IV Universal Continuous Flow Interface (Thermo Fisher Scientific) to an Isotope Ratio Mass Spectrometer (IRMS; Thermo Delta V Advantage, Thermo Fisher Scientific). Calibration was done using certified reference material IAEA-600 ($\delta^{13}C$ = -27.77 ‰; carbon content = 49.49 %) and in-house standards Leucine ($\delta^{13}C$ = -13.73 ‰; carbon content = 54.72 %) and Tuna ($\delta^{13}C$ = -17.96 ‰; carbon content = 45.24 %), which were calibrated against IAEA-600. Values of $\delta^{13}C$ are expressed relative to the international standard Vienna PeeDee Belemnite (VPDB), with a precision for carbon content of <2 % (RSD) and <0.08 ‰ (1 SD) for $\delta^{13}C$. To determine organic carbon content and $\delta^{13}C$, subsamples were weighed into Ag cups and acidified with HCl (10 %, 40 µL or until no further reaction was observed) to remove inorganic carbon. Solid-phase samples were analyzed for inorganic carbon content and associated $\delta^{13}C$ composition using a Gasbench II coupled to an IRMS (Thermo Delta Plus XP, Thermo Fisher Scientific). Calibration was done using certified reference materials LSVEC ($\delta^{13}C$ = -46.60 ‰) and NBS19 ($\delta^{13}C$ = 1.95 ‰) and in-house standards Merck ($\delta^{13}C$ = -9.65 ‰) and Fluka ($\delta^{13}C$ = +2.36 ‰), which were calibrated against LSVEC and NBS19. Values were expressed relative to VPDB, with a precision of <0.1 ‰ (1 SD).

Nutrients were analyzed using a continuous flow analyzer (SAN++, Skalar Analytical). Calibration was done using stock solutions made with NH_4Cl and $NaNO_3$, verified with diluted standard quality control solutions for NH_4^+ (Merck Millipore, reference 1.19812.0500) and NO_3^- (Merck Millipore, reference 1.19811.0500), respectively. The precision (RSD) was 5.9 % (low range) and 0.8 % (high range) for NH_4^+, and 1.5 % (low range) and 1.4 % (high range) for NO_3^-. Dissolved inorganic carbon was analyzed using a DIC analyzer (AS-C6L, Apollo SciTech) coupled to a trace gas analyzer (LI-7810, LICOR). Calibration was done using Dickson certified reference material (batch 209; DIC = 2060.05 µmol kg^{-1}) with a precision (RSD) of 0.16 %. Alkalinity was analyzed using a titrator (Titrando 888, Metrohm) with a 1mL buret. Calibration was done using Dickson certified reference material (batch 209; A_T = 2210.40 µmol kg^{-1}) with a precision (RSD) of 0.08 %. Dissolved pore-water Ca^{2+} was analyzed using an Inductively Coupled Plasma Optical Emission Spectroscopy (ICP-OES) elemental analyzer (AVIO500; Perkin Elmer), using indium as internal standard and the precision was generally <2.5 % (RSD).

https://doi.org/10.5194/egusphere-2026-2930
Preprint. Discussion started: 1 June 2026

2.5 Solute flux calculations

Flux calculations were performed using the R-based software FLUXER, which allows for the calculation of sediment-water fluxes and provides robust data quality checks (Hylén & van de Velde, 2025). Solute fluxes were determined from the linear regression of overlying water concentrations over time.

$$F = \frac{1}{A} \cdot V_{ow} \cdot \frac{dC_{ow}}{dt} = H_{ow} \cdot \frac{dC_{ow}}{dt} \quad (4)$$

V_{ow} is the volume of the overlying water, A is the surface area of the sediment, and C_{ow} is the concentration of the solute in the overlying water. The term V_{ow}/A can be replaced by the height H_{ow} of the overlying water, which was measured once during each session (as the mean of 4 different locations along the circumference of the chamber). Daily measurement of salinity during open incubations indicated no effect of evaporation.

FLUXER assumes simple linear regression by default, but can switch to a quadratic regression model when non-linear trends are detected, for example due to saturation effects from dissolved compound buildup (Devol et al., 1997; Forja & Gómez-Parra, 1998). To evaluate whether a linear of quadratic regression model is appropriate, FLUXER uses the corrected Akaike Information Criterion (cAIC; Hurvich & Tsai, 1989). The regression model with the lowest cAIC was selected, and a difference of >2 was considered to be meaningful (Burnham & Anderson, 2004).

For each model, FLUXER displayed five diagnostic graphs to ensure good model fit and assess whether assumptions for linear regression were fulfilled (Montgomery et al., 2012): (1) residuals versus fitted values, which provided information about data linearity; (2) scale-location plot, which provided information about homoscedasticity; (3) residuals versus time, which provided information about the randomness of errors; (4) normal Q-Q (quantile-quantile) plot, which provided information about the error distribution; and (5) influence plot, which helped to identify points that had a high influence on the model (i.e., outliers) using studentized deleted residuals (SDR), hat values and Cook's distance values as indicators. We refer the reader to the *theoretical background* section of FLUXER for a detailed discussion of how to interpret the diagnostic graphs (Hylén & van de Velde, 2025).

2.6 $CaCO_3$ dissolution rates

Carbonate dissolution rates were calculated using the Keeling plot method (Keeling, 1958, 1961; Pataki et al., 2003), which is based on an isotope mass balance. In closed incubations, the DIC concentration of the overlying water (DIC_{ow}) is the sum of the background DIC concentration at the start of the incubation (DIC_b) and the source DIC concentration (DIC_s), which is added to the overlying water by sedimentary processes:

$$DIC_{ow} = DIC_b + DIC_s \quad (5)$$

$$(\delta^{13}C\text{-}DIC_{ow}) \cdot DIC_{ow} = (\delta^{13}C\text{-}DIC_b) \cdot DIC_b + (\delta^{13}C\text{-}DIC_s) \cdot DIC_s \quad (6)$$

Combining Eq. 5 and Eq. 6 gives a first-order equation in the measured values of δ^{13}C-DIC_{ow} over $1/DIC_{ow}$.

https://doi.org/10.5194/egusphere-2026-2930
Preprint. Discussion started: 1 June 2026

$$\delta^{13}C\text{-}DIC_{ow} = DIC_b \cdot (\delta^{13}C\text{-}DIC_b - \delta^{13}C\text{-}DIC_s) \cdot \left(\frac{1}{DIC_{ow}}\right) + \delta^{13}C\text{-}DIC_s \quad (7)$$

The isotope ratios of source and background can be obtained by a linear regression. The intercept yields δ^{13}C-DIC$_s$. Since there are two sedimentary processes that generate DIC, i.e., organic matter mineralization and $CaCO_3$ dissolution, that each have a distinct isotopic signature, the relative contribution of each process to the total DIC can be derived.

$$f_{OM} + f_{carb} = 1 \quad (8)$$

$$\delta^{13}C\text{-}DIC_s = f_{carb} \cdot \delta^{13}C_{PIC} + f_{OM} \cdot \delta^{13}C_{POC} \quad (9)$$

The fraction of DIC generated by carbonate dissolution hence becomes:

$$f_{carb} = \frac{\delta^{13}C\text{-}DIC_s - \delta^{13}C_{POC}}{\delta^{13}C_{PIC} - \delta^{13}C_{POC}} \quad (10)$$

In these equations, f_{carb} and f_{OM} are the fractions of total DIC derived from $CaCO_3$ dissolution and organic matter mineralization, respectively, while $\delta^{13}C_{PIC}$ and $\delta^{13}C_{POC}$ are the isotopic compositions of $CaCO_3$ and organic matter. At saturation (Ω = 1), the theoretical maximum f_{carb} is 50 %, corresponding to fully efficient metabolic carbonate dissolution, where half of the total DIC pool originates from organic matter mineralization and the other half from $CaCO_3$ dissolution (Eq. 3). Finally, the $CaCO_3$ dissolution rate (R_{diss}) and metabolic $CaCO_3$ dissolution efficiency (MCDE) can be calculated from f_{carb} and the measured DIC flux (F_{DIC}) via:

$$R_{diss} = f_{carb} \cdot F_{DIC} \quad (11)$$

$$MCDE = 2 \cdot f_{carb} \quad (12)$$

Note that our experimental setup precludes any external methane sources.

3 Results

3.1 Sediment properties

The natural sediment had a median grain size of 262 µm and porosity of 0.45 ± 0.03 (n=3) and can be classified as medium sand according to the Wentworth scale. Consistent with a permeable sediment, the organic carbon content was low (0.08 %), while the background level of inorganic carbon was also moderate (0.95 %). Particulate organic carbon (POC) and particulate inorganic carbon (PIC) concentrations of the different substrates used in the experiments (including the added mussel shells) and their corresponding δ^{13}C values are summarized in Table 1.

	POC (wt%)	$\delta^{13}C_{POC}$ (‰)	PIC (wt%)	$CaCO_3$ (wt%)	$\delta^{13}C_{PIC}$ (‰)
Control chamber (n=3)	0.08 ± 0.02	-23.9 ± 0.6	0.95 ± 0.20	7.92 ± 1.67	0.5 ± 1.0
Treatment chamber (n=3)	0.21 ± 0.04	-21.8 ± 0.6	1.95 ± 0.39	16.25 ± 3.25	-0.7 ± 0.6

https://doi.org/10.5194/egusphere-2026-2930
Preprint. Discussion started: 1 June 2026

Mussel shells	2.20	NA	11.12	92.65	NA

Table 1: Particulate organic carbon (POC), particulate inorganic carbon (PIC), and calcium carbonate ($CaCO_3$) concentrations (assuming all PIC is $CaCO_3$) of the sediments in the control and treatment chambers, as well as the added mussel shells. The $\delta^{13}C$ isotopic compositions of the sediments are also provided. Uncertainties are standard deviations based on triplicate chambers. Values for treatment chambers are based on the top layer (2 cm) composition (sediment mixed with crushed mussel shells).

3.2 Sediment-water exchange fluxes

Figure 3a-e shows representative changes with time in overlying water concentrations of different solutes (O_2, DIC, A_T, NO_3^-, and NH_4^+) in the closed and open incubations. Figure 3f-h shows the changes with time in DIC concentration and $\delta^{13}C$-DIC value in a representative closed incubation, as well as the corresponding Keeling plot, displaying the linear regression of $\delta^{13}C$-DIC versus 1/DIC (discussed further in section 3.3). A linear decrease in oxygen saturation was noted during all incubations, with a faster depletion in the treatment chambers (Fig. S1). A linear increase in DIC and A_T concentrations was observed in all incubations, with a faster accumulation in the treatment chambers (Fig. S2 and S3). For A_T, however, the treatment chambers in week 1 displayed a nonlinear trend, with the accumulation rate decreasing halfway through the incubation. For both NO_3^- and NH_4^+, the treatment chambers displayed a clear nonlinear trend in week 1 as seen for A_T (Fig. S4 and S5). Concentrations of NO_3^- remained constant in the beginning of the incubation, after which they increased, while NH_4^+ concentrations increased at the beginning and decreased at the end. After week 1, NO_3^- accumulation strongly decreased until concentrations remained nearly constant over time, while for NH_4^+, no accumulation or depletion over time was observed.

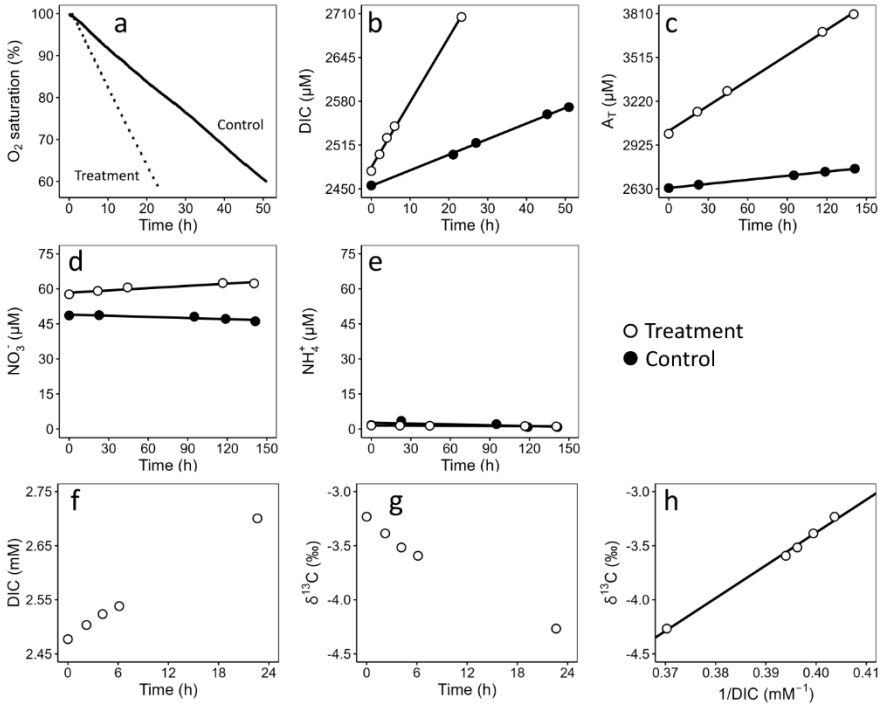

Figure 3: (a–e) Representative overlying water concentration changes with time in a specific accumulation session. (a) Oxygen (O_2, saturation). (b) Dissolved inorganic carbon (DIC). (c) Alkalinity (A_T). (d) Nitrate (NO_3^-). (e) Ammonium (NH_4^+). (f–h) Keeling plot

https://doi.org/10.5194/egusphere-2026-2930
Preprint. Discussion started: 1 June 2026

analysis, here shown for a treatment chamber. (f) Concentrations of DIC in the overlying water. (g) Values of δ^{13}C-DIC in the overlying water. (h) Keeling plot, based on data displayed in panels f and g. The intercept of the linear regression of δ^{13}C-DIC versus 1/DIC shows the relative contribution of carbonate dissolution and organic matter mineralization to the overall DIC pool.

Fluxes of O_2, DIC and A_T were calculated by regression of overlying water concentrations with time, and showed good replication between the replicates at each time point (Fig. 4a-c). Fluxes showed a clear difference between control (F_{O2} = 5.4 ± 1.2 mmol m^{-2} d^{-1}, F_{DIC} = 7.4 ± 1.0 mmol m^{-2} d^{-1}, F_{AT} = 3.2 ± 1.1 mmol m^{-2} d^{-1}; mean flux ± standard deviation over all replicate chambers and flux sessions) and treatment chambers (F_{O2} = 16.8 ± 4.3 mmol m^{-2} d^{-1}, F_{DIC} = 32.0 ± 9.4 mmol m^{-2} d^{-1}, F_{AT} = 25.1 ± 13.5 mmol m^{-2} d^{-1}; Table S1). While fluxes in the control chambers showed little variation over time, the treatment chambers displayed a clear nonlinear trend. Both O_2 (Fig. 4a) and DIC (Fig. 4b) fluxes were initially markedly higher than those of the control chambers, and gradually decreased over the course of the experiment, approaching fluxes of the controls toward the end. Alkalinity fluxes first increased with time until a maximum value of 48.0 ± 6.4 mmol m^{-2} d^{-1} was reached at week 7, after which they decreased and approached the fluxes of the controls toward the end (Fig. 4c). Fluxes of NO_3^- and NH_4^+ in the control chambers were negligible throughout all flux sessions (Table S1). In the treatment chambers, substantial NH_4^+ fluxes were only observed in the first part of week 1 (F_{NH4+} = 5.1 ± 1.5 mmol m^{-2} d^{-1}), while substantial NO_3^- fluxes were only observed in the second part of week 1 (F_{NO3-} = 5.8 ± 1.0 mmol m^{-2} d^{-1}; Table S1). In weeks 3-5, NO_3^- fluxes were still observed, although they were substantially lower (~1 mmol m^{-2} d^{-1}). Finally, flux scatter plots revealed a clear additional DIC source in the treatment chambers beyond mineralization-derived DIC (Fig. 4d), as well as a proportionally greater increase in A_T relative to DIC (Fig. 4e).

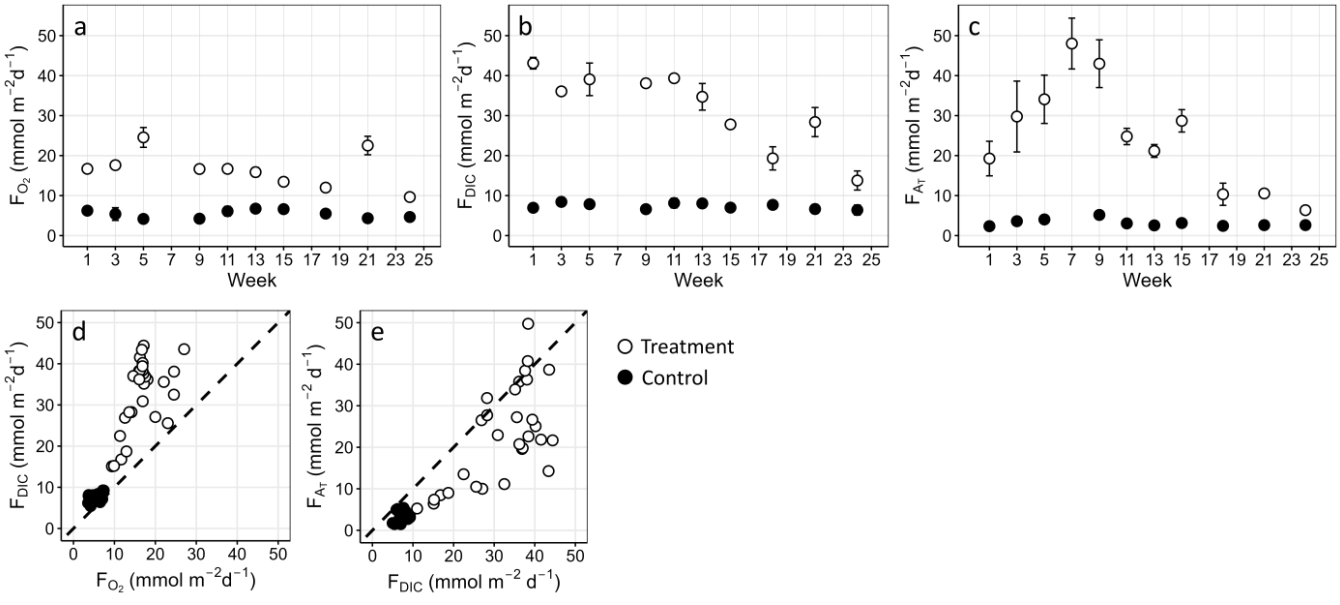

Figure 4: (a) Oxygen fluxes (F_{O2}). (b) Dissolved inorganic carbon fluxes (F_{DIC}). (c) Alkalinity fluxes (F_{AT}). Positive F_{O2} indicate fluxes into the sediment (i.e., net consumption of O_2 by the sediment), positive F_{DIC} and F_{AT} indicate fluxes into the overlying water (i.e., net production of DIC and A_T by the sediment). Means are plotted with error bars representing standard deviations based on three

https://doi.org/10.5194/egusphere-2026-2930
Preprint. Discussion started: 1 June 2026

replicate chambers. No O_2 and DIC data were available for week 7, as only open incubations were performed during that week. (d) 1:1 plot, comparing F_{DIC} and F_{O2}. (e) 1:1 plot, comparing F_{AT} and F_{DIC}.

3.3 $CaCO_3$ dissolution rates

Figure 5a-b and Table S2 show the derived f_{carb} and corresponding R_{diss} values for all weeks (see Fig. S6 for all Keeling plots and Table S2 for all model intercepts and p-values). A nonlinear trend was observed in the treatment chambers over the course of the experiment, with f_{carb} and R_{diss} increasing over time, reaching a maximum of f_{carb} = 59.5 ± 6.5 % (R_{diss} = 22.7 ± 2.6 mmol m^{-2} d^{-1}) in week 9, followed by a gradual decrease toward a final f_{carb} of 17.3 ± 12.7 % (R_{diss} = 2.2 ± 1.1 mmol m^{-2} d^{-1}). In the control chambers, f_{carb} remained relatively stable over time, although some variability was observed both among replicate chambers and across incubation weeks. As the Keeling plot method combines measurements of both DIC and δ^{13}C-DIC, each with associated uncertainties, such variability is expected, particularly in control chambers, where concentration and isotopic composition changes over time are relatively small. The occurrence of negative f_{carb} values in some control chambers indicated that the regression intercept fell outside the isotopic range defined by the $CaCO_3$ and organic matter end-members. This has no geochemical meaning, other than suggesting that little to no $CaCO_3$ dissolution is occurring, and underscores the uncertainty that the Keeling plot approach inherently incorporates when variations in DIC and/or δ^{13}C-DIC are relatively modest. For this reason, R_{diss} was only calculated for chambers with positive f_{carb} values (Fig. 5b).

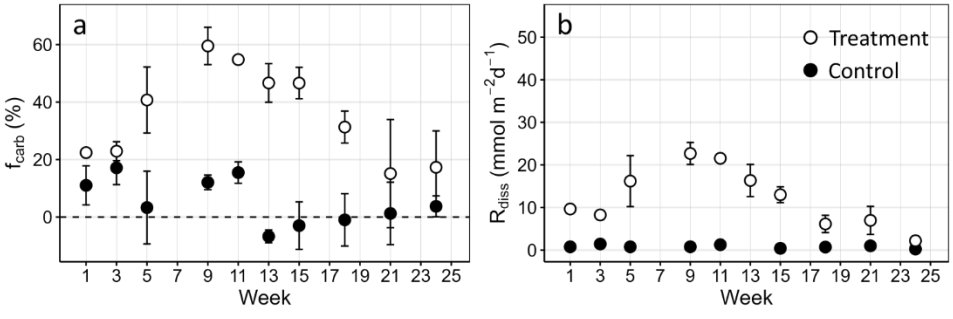

Figure 5: (a) Mean fraction of total DIC derived from $CaCO_3$ dissolution (f_{carb}) as determined using the Keeling plot method. (b) Corresponding mean $CaCO_3$ dissolution rates (R_{diss}). Valued of R_{diss} were only calculated for positive values of f_{carb}, as discussed in the main text. Error bars are standard deviations based on three replicate chambers.

3.4 Pore-water geochemistry

We tracked the color changes in the sediment over time by taking time lapse photographs (Fig. S7). These images reveal a markedly different color evolution in control versus treatment, thus suggesting a different development of the geochemistry. In the controls, the sediment remained light-grey colored, and the only color change observed was the development of a thin (~5 mm) orange layer just below the sediment-water interface (Fig. S7). This feature suggests remobilization of ferrous iron in deeper layers, which then precipitates out as iron (hydr)oxide upon upward diffusion and contact with O_2. In contrast, in the treatments, there was a far more notable color change, as the entire layer with mussel shell fragments became black over the course of the first three weeks (Fig. S7), thus suggesting precipitation of iron sulfides. As the

https://doi.org/10.5194/egusphere-2026-2930
Preprint. Discussion started: 1 June 2026

experiment progressed, this black layer became gradually grey again (first starting from the top), thus indicating oxygenation and reoxidation of iron sulfides. This distinct geochemical trajectory of control versus treatment chambers, was confirmed by the pore-water analysis at the end of the experiment.

Figure 6 displays the depth profiles in pore-water concentrations (Ca^{2+}, DIC) and isotopic composition ($\delta^{13}C$-DIC) recorded at the end of the experiment. Higher pore-water Ca^{2+} concentrations were observed in the treatment chambers as compared to the control chambers (Fig. 6a). In the control chambers, pore-water Ca^{2+} concentrations remained constant with depth, and were similar to the concentration of ~9.5 mM of the overlying seawater. In contrast, in the treatment chambers, dissolved Ca^{2+} markedly increased with depth, reaching 12-13 mM at 12 cm depth. Pore-water DIC profiles showed an increasing trend with sediment depth for both control and treatment chambers, but with a different shape and higher DIC concentrations observed in the treatment chambers (Fig. 6b). Profiles of $\delta^{13}C$-DIC showed a decreasing trend in $\delta^{13}C$ values with sediment depth in the control chambers. In the treatment chambers, however, $\delta^{13}C$ values decreased in the top layer but then remained relatively stable below a depth of ~1 cm (Fig. 6c). Pore-water 1:1 plots of Ca^{2+} and DIC concentrations revealed a clear Ca^{2+} source in the treatment chambers, alongside higher DIC production (Fig. 6d). It should be noted that pore-water samples were only taken once at the end of the experiment (24 weeks), which allowed for the downward buildup of solutes over time. This should be accounted for in the interpretation of the depth profiles. For example, if $CaCO_3$ dissolution only occurs in the oxygenated top layer in the treatment chambers, downward diffusion can lead to elevated concentrations in deeper anoxic layers. Likewise, the overlying water was replaced after every incubation. This enables upward diffusive and advective transport of Ca^{2+} into the overlying water, thus resulting in a lower buildup in the top layer.

https://doi.org/10.5194/egusphere-2026-2930
Preprint. Discussion started: 1 June 2026

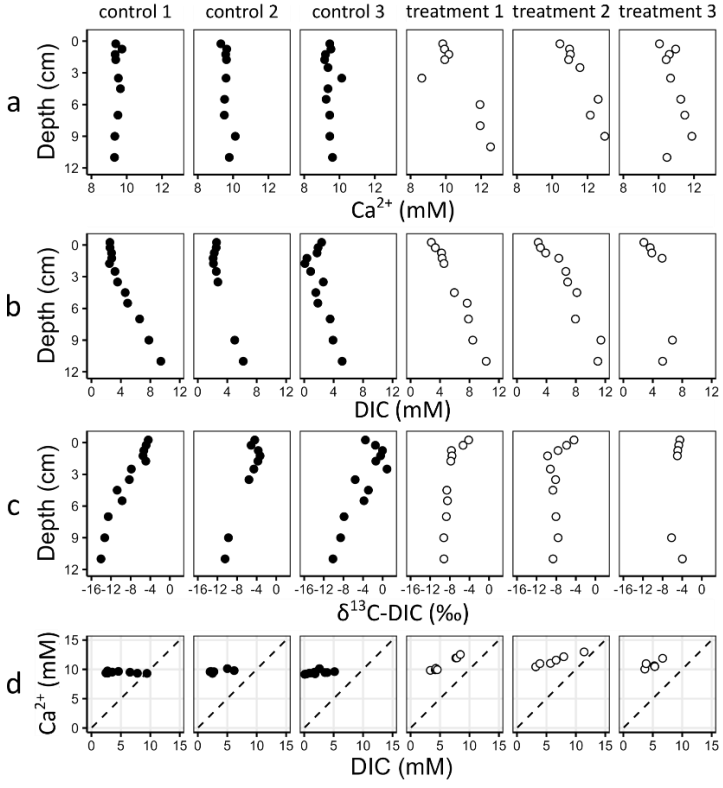

Figure 6: Pore-water profiles. (a) Dissolved inorganic carbon (DIC). (b) Isotopic DIC composition (δ^{13}C-DIC). (c) Calcium (Ca^{2+}). (d) 1:1 plot, comparing Ca^{2+} and DIC concentrations. Pore-water samples were only taken once at the end of the experiment, explaining the buildup of solutes in deeper anoxic layers, as further discussed in the main text.

4 Discussion

4.1 Mussel shell dissolution provides a significant additional A_T source

Metabolic $CaCO_3$ dissolution is thought to occur more efficiently in oxygenated sediments, where the aerobic mineralization of organic matter produces the CO_2 that drives the pore water toward undersaturation (Archer et al., 1989; Emerson & Bender, 1981; Lunstrum & Berelson, 2022; Morse et al., 1985). To meet this condition, permeable sediment (medium sand; porosity 0.45) was used here in the experiment. While the natural sediment employed does contain a sizeable baseline amount of PIC (0.95 ± 0.20 %; Table 1), low A_T fluxes were observed in the control chambers (Fig. 4c). Likewise, the Keeling plot analysis revealed low rates of metabolic carbonate dissolution (Fig. 5b). The mean $CaCO_3$ dissolution rate of 0.9 ± 0.5 mmol m^{-2} d^{-1} as observed in the controls, corresponds to an A_T flux 1.8 ± 1.0 mmol m^{-2} d^{-1}, thus providing ~56 % of the total measured A_T flux of 3.2 ± 1.1 mmol m^{-2} d^{-1}. The low organic carbon content of the natural sediment (0.08 ± 0.02 wt%; Table 1) resulted in low mineralization rates, as indicated by the low O_2 consumption rates (Fig. 4a), which are a proxy

https://doi.org/10.5194/egusphere-2026-2930
Preprint. Discussion started: 1 June 2026

for total sedimentary organic matter mineralization (Glud, 2008; Jørgensen et al., 2022). The low CO_2 production from mineralization thus constrained metabolic $CaCO_3$ dissolution in the natural sediment.

In the treatment chambers, more favorable conditions for metabolic dissolution were established, as the added mussel shells still had a considerable amount of associated organic matter (2.20 wt%; Table 1), which stimulated organic matter mineralization, as reflected in the O_2, DIC and A_T fluxes (Fig. 4a-c). First, elevated O_2 fluxes in the treatment chambers suggest high mineralization rates driven by the organic matter associated with the shells, and thus an increased metabolic dissolution potential. Second, elevated DIC fluxes in the treatment chambers confirmed increased metabolic dissolution driven by the more intense mineralization (Fig. 4d). The Keeling plot analysis demonstrates there is a clear additional DIC source coming from $CaCO_3$ dissolution in the treatment chambers (Fig. 5b), which is further supported by the higher Ca^{2+} and DIC pore-water concentrations observed in the treatment chambers (Fig. 6a-b, Fig. 6d). Third, high A_T fluxes in the treatment chambers (Fig. 4c; Fig. 4e) also provide support for substantial $CaCO_3$ dissolution, as 2 mol of A_T are produced per mol of $CaCO_3$ dissolved (Eq. 1). In addition, comparison of the A_T fluxes attributed to $CaCO_3$ dissolution (as derived from the Keeling plot analysis) with the total A_T fluxes (as measured in the overlying water) revealed a strong linear correlation for nearly all flux sessions (Fig. 7a-b), demonstrating that $CaCO_3$ dissolution was the dominant A_T source in the treatment chambers. In week 3, the measured A_T flux exceeded the A_T flux attributed to $CaCO_3$ dissolution, indicating an additional A_T source, while in weeks 11 and 13, the opposite was observed, indicating the presence of an A_T sink (Fig. 7a-b).

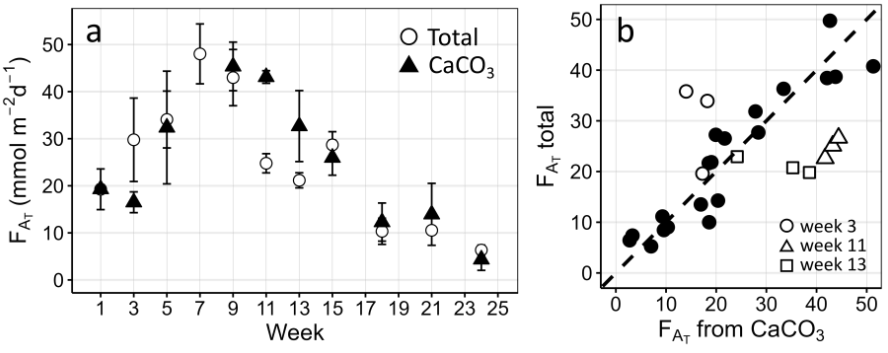

Figure 7: Shell-amended chamber flux comparison of total A_T, which was measured directly in the overlying water, and $CaCO_3$ A_T, which was derived using the Keeling plot analysis. a) Mean weekly fluxes with standard deviations based on three replicate chambers. b) 1:1 plot, comparing the individual weekly total and $CaCO_3$-derived A_T fluxes per chamber.

4.2 Factors controlling metabolic $CaCO_3$ dissolution

The observed geochemistry in the treatment chambers carries a clear signature of metabolic $CaCO_3$ dissolution. Given that metabolic $CaCO_3$ dissolution is constrained by the availability of oxygen, organic matter, and $CaCO_3$ (Eq. 3), an important question is which of these three factors acts as the primary limiting factor. Metabolic carbonate dissolution efficiencies (MCDE, Eq. 12) offer a useful metric to assess this issue. Efficiencies <100 % can be due to different processes: (1) the $CaCO_3$ pool is either too small or not reactive enough for dissolution to fully utilize the potential of mineralization, (2) the pore water receives alkalinity from anaerobic mineralization processes, which suppresses the undersaturation with respect to $CaCO_3$

https://doi.org/10.5194/egusphere-2026-2930
Preprint. Discussion started: 1 June 2026

(Soetaert et al., 2007), or (3) the acid (i.e. CO_2) produced by aerobic mineralization is flushed out of the pore water by advective transport before it can drive the pore water toward undersaturation (Goossens et al., 2026).

4.2.1 Limitation by $CaCO_3$ availability and reactivity

To assess whether $CaCO_3$ availability limited dissolution in the treatment chambers, the total amount of $CaCO_3$ dissolved over the course of the experiment was calculated by integrating the R_{diss} values obtained from the Keeling plot analysis over their respective incubation periods and the sediment surface area (Fig. 5b). This resulted in a total of 6.1 ± 1.2 g of $CaCO_3$ dissolved, corresponding to 6.1 ± 1.2 % of the initial shell mass that was added. These results suggest that $CaCO_3$ availability most likely did not limit dissolution.

In addition to $CaCO_3$ content as such, $CaCO_3$ dissolution efficiency can also be limited by reactivity. When pore waters transition from over- to undersaturated conditions, carbonate minerals dissolve more readily at high-energy surface sites such as steps and kinks, which are more reactive than smoother surfaces (Adkins et al., 2021). In this experiment, mussel shells were freshly crushed, resulting in higher surface impurities relative to the natural $CaCO_3$ present in the sediment. This suggests that $CaCO_3$ reactivity was unlikely to be limiting carbonate dissolution in the shell-amended chambers.

4.2.2 Limitation by anaerobic mineralization and pore-water flushing

Undersaturation of pore waters with respect to $CaCO_3$ can only be achieved under oxic conditions. In coarse sediments, this is stimulated by advection, which allows deeper oxygen penetration (Huettel & Gust, 1992) and increases the zone in which $CaCO_3$ undersaturation can develop. The degree of undersaturation is further controlled by the pore-water residence time (PRT), which is the mean time that seawater remains within the sediment before being replaced by new overlying water. If the PRT is too short, acid produced by aerobic mineralization is flushed out before it can drive the pore water toward undersaturation. If the PRT is too long, alkalinity from $CaCO_3$ dissolution will accumulate and drive the pore water back toward saturation (Goossens et al., 2026).

Below the oxic zone, anaerobic mineralization generates alkalinity instead of acidity, along with reduced metabolites (Soetaert et al., 2007). However, these reduced compounds are typically transported upward into the oxic zone, where their reoxidation produces acidity that lowers the $CaCO_3$ saturation state of the pore water. This means that metabolic carbonate dissolution can occur directly via aerobic mineralization and indirectly via anaerobic mineralization coupled to reoxidation in the oxic zone. Iron sulfide precipitation, however, represents an exception to this process. When hydrogen sulfide (H_2S), formed during sulfate reduction, reacts with reactive iron and precipitates as iron sulfide, the upward transport of H_2S and its subsequent reoxidation is prevented, leading to a net source of alkalinity (Hu & Cai, 2011; Middelburg et al., 2020). Under such conditions, the efficiency of metabolic carbonate dissolution is reduced since a potential source of acidity from mineralization is removed.

Ultimately, the interplay between aerobic/anaerobic mineralization and pore-water exchange dictates whether pore waters become under- or oversaturated, thus controlling the MCDE. Throughout the experiment, three distinct phases can be

https://doi.org/10.5194/egusphere-2026-2930
Preprint. Discussion started: 1 June 2026

distinguished (Fig. 8). During the first phase (week 1-9), $CaCO_3$ dissolution appeared to be limited by oxygen availability, resulting in initial low MCDE values that gradually increased over time. During the second phase (weeks 9-15), the full dissolution efficiency (MCDE ≈ 100 %) was attained. In the third and final phase (weeks 15-24), the MCDE decreased again with time.

During the first phase of the experiment (week 1-9), intense mineralization took place, likely driven by the fresh organic matter associated with the mussel shells. This process was immediately visibly apparent, as during the first week, the top layer of the shell-amended sediment (where the mussel shell fragments had been added) turned black, indicative of sediment anoxia and iron sulfide formation (Fig. S7). The oxygen consumption in the treatment chambers was high, suggesting that the oxic zone was likely strongly diminished. Session 1 was also the only session that we observed NH_4^+ accumulation in the overlying water, suggesting that nitrification was inhibited, most likely by a lack of oxygen. In all ensuing flux sessions, the NH_4^+ efflux from the sediment remained negligible (Table S1). In the latter part of week 1, oxic conditions apparently reestablished, as nitrification initiated, leading to a depletion of NH_4^+ (Fig. S5) and a buildup of NO_3^- (Fig. S4). Nitrification consumes A_T by releasing protons, thus explaining the observed nonlinear A_T accumulation in week 1. Anaerobic mineralization generates alkalinity, which elevates the $CaCO_3$ saturation state in the pore water, thus explaining the low $CaCO_3$ dissolution efficiency (~45 %) observed in week 1.

In the rest of the first phase (after week 1), the mineralization remained high (as indicated by high O_2 and DIC fluxes; Fig. 4a-b), but the pore waters recovered from the initial "mineralization burst" and became gradually more oxygenated, stimulating metabolic $CaCO_3$ dissolution (Eq. 3). As a result, the MCDE increased with time, until reaching its maximum value in week 9.

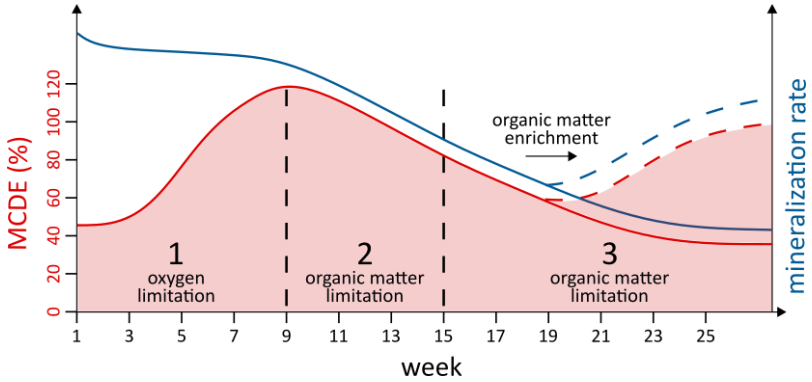

Figure 8: Conceptual figure illustrating the three distinct phases observed after mussel shell amendment. Oxygen availability limits $CaCO_3$ dissolution efficiency during phase 1. During phase 2, $CaCO_3$ dissolution is limited by organic matter (OM) availability, while occurring at maximum efficiency. During phase 3, dissolution efficiency is limited by OM availability. A new quasi-steady state is achieved, with dissolution efficiencies and rates slightly higher than those observed in sediments without added shells. In a real-world shell amendment scenario, however, metabolic $CaCO_3$ dissolution is continuously fueled by the supply of fresh OM from the water column, potentially driving the system back toward maximum efficiency.

During the second phase (weeks 9-15), carbonate dissolution occurred at maximum efficiency in the shell layer, as reflected in the $\delta^{13}C$-DIC pore-water profiles, where organic matter ($\delta^{13}C$ = -21.8 ‰) and $CaCO_3$ ($\delta^{13}C$ = -0.7 ‰) contributed

https://doi.org/10.5194/egusphere-2026-2930
Preprint. Discussion started: 1 June 2026

equally to the δ^{13}C-DIC pool, as observed by the build-up of a constant value of ~-10 ‰ in the deeper layers (Fig. 6c). The sediment is thus characterized by a maximum metabolic carbonate dissolution efficiency (MCDE ≈ 100 %; Fig. 8). Maximum efficiencies indicate that R_{min} in the shell layer was sufficiently large to overwhelm any effect of iron sulfide formation below the oxic layer on f_{carb}.

In week 9-11, the MCDE efficiency even exceeded 100 % (Fig. 8). Theoretically, this is not possible when only metabolic dissolution is at play, but it can occur when an additional acid source is present. The observed MCDE efficiencies >100 % are hence either related to uncertainty in their estimation, or they can also result from the transient reoxidation of a pool of iron sulfides, a process which generates acid and consumes A_T (Rimstidt & Vaughan, 2003). After week 9, the intensity of mineralization decreased, which may have caused an increased and deeper oxygenation, and hence, a reoxidation of previously accumulated iron sulfides.

During the third phase (weeks 15-24), MCDE decreased with time (Fig. 8). At this point, the most labile fraction of organic matter had been mineralized, leading to reduced mineralization rates and decreased O_2 consumption rates (Fig. 4a). At this point, carbonate dissolution likely became limited by organic matter availability, and dissolution rates decreased accordingly (Fig. 5b). The decreasing R_{min} could not generate sufficient acidity to drive the pore water fully toward undersaturation before being flushed, thereby reducing R_{diss}, f_{carb} and MCDE. Eventually, the treatment chambers appeared to evolve toward a new quasi-steady state, with R_{diss} being slightly higher than those in the control chambers (Fig. 5b).

At the end of the experiment, carbonate dissolution appeared limited by organic matter availability. We hence speculate that the addition of new fresh organic matter could again increase the dissolution rate and associated MCDE (Fig. 8). The latter aspect was not examined in the current experiment but provides a testable hypothesis for future studies.

4.3 Enhanced $CaCO_3$ dissolution in the global aquaculture context

The flux incubations performed here provide estimates for the areal $CaCO_3$ dissolution rate and A_T flux induced by enhanced mussel shell dissolution. These values can be used to arrive at a first-order estimate of the potential of bivalve dissolution approaches within an OAE context. When extrapolating our results to the global aquaculture context, we need to consider both CO_2 emissions associated with mussel shell aquaculture as well as CO_2 sequestration obtained from a shell amendment scenario.

Global yearly CO_2 emissions (m_{CO_2}; ton CO_2 yr^{-1}) associated with calcification in mussel aquaculture can be calculated as:

$$m_{CO_2} = m_{mussel} \cdot x_{shell} \cdot x_{CaCO_3} \cdot \psi \cdot \frac{M_{CO_2}}{M_{CaCO_3}} \quad (12)$$

In this, m_{mussel} represents the total mass of harvested mussels from aquaculture (ton per year), x_{shell} denotes the shell fraction of the total mussel mass (~29 %; Adler et al., 2024), x_{CaCO_3} represents the $CaCO_3$ fraction of shells (92.65 %; Table 1), ψ is the molar ratio of CO_2 released versus $CaCO_3$ precipitated (Frankignoulle, 1994; Frankignoulle et al., 1994), and M_{CO_2} and

https://doi.org/10.5194/egusphere-2026-2930
Preprint. Discussion started: 1 June 2026

M_{CaCO_3} are the molar masses of CO_2 (44.01 g mol^{-1}) and $CaCO_3$ (100.01 g mol^{-1}), respectively. Calculation of ψ was done using the CRAN:seacarb package in R software (Gattuso et al., 2024), with input parameters representative of surface seawater conditions: DIC = 2100 µmol kg^{-1}, salinity = 35, temperature = 15°C, and atmospheric pCO_2 = 427 µatm (Lan et al., 2025). This yielded a value of ψ = 0.72. Blue mussel aquaculture has a global production of approximately 132 kton per year (FAO, 2025), and so, the CO_2 emissions linked to calcification are ~11.2 kton CO_2 yr^{-1}. Using the results obtained here, 6.1 ± 1.2 % of the initial shell mass was dissolved after 24 weeks, and so the corresponding CO_2 compensation over the same time period would be 6.1 % of the calcification-related emissions incurred during the growth phase (representing 686 ± 135 ton CO_2 globally). It should be noted, however, that at the end of the experimental period, the $CaCO_3$ dissolution rate and corresponding A_T flux in the treatment chambers were still higher than those in the control chambers, thus indicating that enhanced shell dissolution would still continue for a longer period. Assuming the dissolution rate stays constant in time, it would take ~38 years to completely dissolve the added mussel shell fragments, if we use the (quasi-steady-state) dissolution rate measured at the end of the experiment. Alternatively, if we use the average dissolution rate over the experiment, this timescale reduces to ~7 years.

Furthermore, our results clearly indicate that carbonate dissolution was limited by organic matter availability from week ~15 onward, leading to lowered mineralization rates and decreased metabolic $CaCO_3$ dissolution. Such a depletion of the fresh organic matter is a direct consequence of the incubation procedure. In real-world application scenarios, fresh organic matter would be continuously supplied from the water column, especially during spring blooms (Fig. 8). As a result, this would fuel metabolic $CaCO_3$ dissolution and hence reduce the dissolution time of bivalve shell material. As such, the potential of mussel-shell amendment as a strategy to compensate for aquaculture CO_2 emissions could be greater than suggested by our laboratory experiment. This is supported by a recent study, which simulated an application scenario of two types of biominerals to coastal sediments by means of a reactive transport model. These simulations showed that enhanced A_T production from shell dissolution could be sustained for over 30 years before transitioning back to steady state (Biçe et al., 2025). Sensitivity analysis also confirmed the limiting effect of lowered mineralization rates on $CaCO_3$ dissolution rates, supporting our findings that shell amendment would be most effective in environments with high organic matter degradation (Biçe et al., 2025).

Enhanced bivalve shell dissolution is most promising in $CaCO_3$-poor permeable sediments residing in shallow areas with high local primary production. Globally, ~70 % of the continental shelf sediments are classified as sandy (i.e. permeable; Burdige, 2007), while ~88 % is classified as $CaCO_3$-poor (Smith & Mackenzie, 2016), thus showing that the coastal environment has a large areal potential for OAE applications based on enhanced bivalve shell dissolution. Bivalve aquaculture produces approximately 12 million tons of shell material per year (FAO, 2025), which at the concentrations employed here (8 % addition) would require ~5000 km^2 of new application area per year. This area only represents 0.04 % of the $CaCO_3$-poor, sandy sediments found on the global continental shelf, and hence, the space for application does not appear to be limiting.

Still, the selection of an application site for enhanced bivalve shell dissolution requires judicious consideration. Sandy sediments are generally low in organic matter content, and so their potential for metabolic $CaCO_3$ dissolution is highly dependent on a continuous local input of organic matter (de Beer et al., 2005; Goossens et al., 2026). Therefore, sandy sites

https://doi.org/10.5194/egusphere-2026-2930
Preprint. Discussion started: 1 June 2026

with a suitably increased flux of organic matter toward the seabed seem preferential. When the organic matter input is too low, metabolic carbonate dissolution becomes limited by organic matter. Likewise, when organic matter inputs are too high, metabolic carbonate dissolution can become oxygen limited. Intensified mineralization can deplete sediment oxygen and create sulfidic conditions, which promotes alkalinity production by iron sulfide formation. Likewise, intensified mineralization can remove the presence of bioturbating infauna (Christensen et al., 2003), which enhance the oxygenation of the pore water through bio-irrigation (Aller, 1980), thus pumping oxygen-rich water into deeper anoxic layers (Meysman et al., 2006). Under such circumstances, $CaCO_3$ dissolution shifts from being organic-matter-limited to being oxygen-limited.

One potential application scenario could be to redistribute shell waste in or near mussel aquaculture environments, which are known to have induced high organic matter deposition rates (Christensen et al., 2003; Hargrave et al., 2008; Lavoie et al., 2024). This would also create direct compensation for the calcifying-induced CO_2 emissions that are locally generated (i.e. within-project offsetting). Moreover, it could potentially also improve aquaculture conditions by releasing alkalinity and increasing the seawater pH, although this effect will strongly depend on the residence time of the water at the site. Previous studies have investigated organic matter accumulation beneath mussel farms and its effect on the local sediment geochemistry, showing that the magnitude of the impact depends on multiple factors. While the mussel density determines the total organic matter flux from the water column, the distance from the farm and the local hydrodynamics control how much of this material is deposited within the sediment (e.g., Christensen et al., 2003; Cranford et al., 2007; Hargrave et al., 2008; Lacoste et al., 2018; Lavoie et al., 2024; McKindsey et al., 2011; Wilson & Vopel, 2015). This emphasizes the need to carefully characterize sediment conditions prior to mussel shell waste application. Optimal sites could be areas with low hydrodynamic forcing that are located near but not directly beneath mussel farms, allowing elevated organic matter deposition without inducing anoxia, or areas with high hydrodynamic forcing directly beneath mussel farms, where organic matter fluxes are high but sufficiently dispersed to prevent highly localized deposition.

5 Summary and outlook

In this study, we investigated the dissolution of mussel shell waste in permeable sediments as a novel type of OAE approach, which aims for enhanced circularity and reduced emissions in bivalve aquaculture operation. While mussels (and bivalves in general) have already a low CO_2 footprint per gram of protein compared to other food sources, this CO_2 footprint could be lowered by dissolving the shells in marine conditions. Permeable sediment amended with crushed mussel shells exhibited significantly higher dissolution rates, driven by aerobic mineralization linked to organic matter associated with the shells. A transient dissolution pattern was observed, where initial oxygen limitation was followed by organic matter limitation. After 24 weeks of sediment incubation, 6.1 ± 1.2 % of the initial shell mass had dissolved, which upon extrapolation provides a dissolution timescale of ~38 years. Deploying mussel shell waste in natural sediments with high and continuous organic matter deposition, however, could increase the compensation potential and shorten the dissolution timescale. Potential application areas include mussel farms, which would allow for direct in-project CO_2 compensation, with the potential of

https://doi.org/10.5194/egusphere-2026-2930
Preprint. Discussion started: 1 June 2026

improving aquaculture conditions. Careful characterization of the sediment geochemistry prior to mussel shell waste application is crucial to ensure optimal conditions for $CaCO_3$ dissolution.

While enhanced mussel shell dissolution seems feasible, it should be noted that the results presented here are derived from a controlled laboratory experiment. In contrast, natural sediments experience seasonal variation in temperature and organic matter deposition, are subject to variable hydrodynamic forcing (including storms), and experience infaunal activity such as bioturbation and bio-irrigation, all of which can influence oxygen availability or benthic mineralization rates. Bridging the gap between laboratory and field conditions will require experiments conducted under more realistic settings, such as large-scale mesocosms and eventually field trails. To date, OAE studies are heavily inclined toward modeling approaches. While models are crucial for exploring large-scale scenarios, their predictive capacity ultimately depends on experimental data, which is currently still largely lacking. In this study, we tested a single mussel shell loading in a single sediment type under controlled conditions. It remains unknown whether higher shell concentrations could yield a higher CO_2 compensation potential, or how this potential might change in coarser sediments with deeper oxygen penetration. Future research exploring a range of shell waste types, loadings and sediment grain sizes in realistic field conditions is needed to identify the optimal conditions for enhanced shell dissolution.

Code availability

The code used for analysis in this study is available upon request. Interested parties may contact the corresponding author.

Data availability

The raw data is publicly available on GitHub and archived on Zenodo at https://doi.org/10.5281/zenodo.19632016.

Author contributions

CG conducted the experiment and was responsible for the data collection, analysis, and writing of the manuscript. SJVDV and FJRM were responsible for the conceptualization and supervision of the study. SB supervised analysis of solid phase and δ^{13}C-DIC samples. All authors contributed to the final manuscript.

Competing interests

At least one of the (co-)authors is a member of the editorial board of Biogeosciences.

https://doi.org/10.5194/egusphere-2026-2930
Preprint. Discussion started: 1 June 2026

Acknowledgements

The authors thank Gunter Flipkens and Nada Nasri for assistance during pore-water sampling, Greet Lembregts for assistance during pore-water sampling and analysis of samples, and Yannick Stroobandt for analysis of samples.

Financial support

This research was supported by the RV/21/DEHEAT project from the Belgian Science Policy Office (BELSPO), a Strategic Basic Research (SBO) project (no. S000619N) from Research Foundation Flanders (FWO), and the Blue Cluster project (project no. HBC.2023.0496) from Flanders Innovation & Entrepreneurship (VLAIO). Cedric Goossens was supported by a University Research Fund (BOF) of the University of Antwerp. Sebastiaan J. van de Velde acknowledges the New Zealand MBIE Strategic Science Investment Fund for support via the ESNZ Ocean-Climate Interaction programme.

References

Adkins, J. F., Naviaux, J. D., Subhas, A. V., Dong, S., & Berelson, W. M. (2021). The Dissolution Rate of $CaCO_3$ in the Ocean. *Annual Review of Marine Science*, *13*(1), 57–80. https://doi.org/10.1146/annurev-marine-041720-092514

Adler, I., Kotta, J., Robal, M., Humayun, S., Vene, K., & Tuvikene, R. (2024). Valorization of Baltic Sea farmed blue mussels: Chemical profiling and prebiotic potential for nutraceutical and functional food development. *Food Chemistry: X*, *23*, 101736. https://doi.org/10.1016/j.fochx.2024.101736

Aller, R. C. (1980). Quantifying solute distributions in the bioturbated zone of marine sediments by defining an average microenvironment. *Geochimica et Cosmochimica Acta*, *44*, 1955–1965. https://doi.org/10.1016/0016-7037(80)90195-7

Archer, D., Emerson, S., & Reimers, C. (1989). Dissolution of calcite in deep-sea sediments: pH and O2 microelectrode results. *Geochimica et Cosmochimica Acta*, *53*(11), 2831–2845. https://doi.org/10.1016/0016-7037(89)90161-0

Biçe, K., Myers Stewart, T., Waldbusser, G. G., & Meile, C. (2025). The effect of carbonate mineral additions on biogeochemical conditions in surface sediments and benthic–pelagic exchange fluxes. *Biogeosciences*, *22*(3), 641–657. https://doi.org/10.5194/bg-22-641-2025

Bullock, L. A., James, R. H., Matter, J., Renforth, P., & Teagle, D. A. H. (2021). Global Carbon Dioxide Removal Potential of Waste Materials From Metal and Diamond Mining. *Frontiers in Climate*, *3*, 694175. https://doi.org/10.3389/fclim.2021.694175

Burdige, D. J. (2007). Preservation of organic matter in marine sediments: Controls, mechanisms, and an imbalance in sediment organic carbon budgets? *Chemical Reviews*, *107*(2), 467–485. https://doi.org/10.1021/cr050347q

Burnham, K. P., & Anderson, D. R. (Eds.). (2004). *Model Selection and Multimodel Inference*. Springer New York. https://doi.org/10.1007/b97636

Carlson, R. R., Lewis, M. A., Ninokawa, A. T., Saley, A. M., Hill, T. M., & Gaylord, B. (2025). Shell dissolution rates differ fourfold between mussel species. *Royal Society Open Science*, *12*(7), 250664. https://doi.org/10.1098/rsos.250664

Christensen, P. B., Glud, R. N., Dalsgaard, T., & Gillespie, P. (2003). Impacts of longline mussel farming on oxygen and nitrogen dynamics and biological communities of coastal sediments. *Aquaculture*, *218*(1–4), 567–588. https://doi.org/10.1016/S0044-8486(02)00587-2

Cranford, P., Strain, P., Dowd, M., Hargrave, B., Grant, J., & Archambault, M. (2007). Influence of mussel aquaculture on nitrogen dynamics in a nutrient enriched coastal embayment. *Marine Ecology Progress Series*, *347*, 61–78. https://doi.org/10.3354/meps06997

https://doi.org/10.5194/egusphere-2026-2930
Preprint. Discussion started: 1 June 2026

Cubillas, P., Köhler, S., Prieto, M., Chaïrat, C., & Oelkers, E. H. (2005). Experimental determination of the dissolution rates of calcite, aragonite, and bivalves. *Chemical Geology*, *216*(1–2), 59–77. https://doi.org/10.1016/j.chemgeo.2004.11.009

de Beer, D., Wenzhöfer, F., Ferdelman, T. G., Boehme, S. E., Huettel, M., Van Beusekom, J. E. E., Böttcher, M. E., Musat, N., & Dubilier, N. (2005). Transport and mineralization rates in North Sea sandy intertidal sediments, Sylt-Rømø Basin, Wadden Sea. *Limnology and Oceanography*, *50*(1), 113–127. https://doi.org/10.4319/lo.2005.50.1.0113

Devol, A. H., Codispoti, L. A., & Christensen, J. P. (1997). Summer and winter denitrification rates in western Arctic shelf sediments. *Continental Shelf Research*, *17*(9), 1029–1050. https://doi.org/10.1016/S0278-4343(97)00003-4

Dickson, A. G. (1981). An exact definition of total alkalinity and a procedure for the estimation of alkalinity and total inorganic carbon from titration data. *Deep-Sea Research*, *28A*(6), 609–623. https://doi.org/10.1016/0198-0149(81)90121-7

Emerson, S., & Bender, M. (1981). Carbon fluxes at the sediment-water interface of the deep-sea: Calcium carbonate preservation. *Journal of Marine Research*, *39*(1). https://elischolar.library.yale.edu/journal_of_marine_research/1537

Ericson, J. A., & Ragg, N. L. C. (2022). Effects of crushed mussel, *Perna canaliculus* , shell enrichment on seawater carbonate buffering and development of conspecific larvae exposed to near-future ocean acidification. *Journal of the World Aquaculture Society*, *53*(1), 271–289. https://doi.org/10.1111/jwas.12779

FAO. (2024). *The State of World Fisheries and Aquaculture 2024—Blue Transformation in action*. FAO. https://doi.org/10.4060/cd0683en

FAO. (2025). *FishStat: Global aquaculture production 1950-2023. [Accessed on 28 March 2025]. In: FishStatJ. Available at www.fao.org/fishery/en/statistics/software/fishstatj. Licence: CC-BY-4.0* [Computer software].

Flipkens, G., Fuhr, M., Fiers, G., Meysman, F. J. R., Town, R. M., & Blust, R. (2023). Enhanced olivine dissolution in seawater through continuous grain collisions. *Geochimica et Cosmochimica Acta*, *359*, 84–99. https://doi.org/10.1016/j.gca.2023.09.002

Forja, J., & Gómez-Parra, A. (1998). Measuring nutrient fluxes across the sediment-water interface using benthic chambers. *Marine Ecology Progress Series*, *164*, 95–105. https://doi.org/10.3354/meps164095

Frankignoulle, M. (1994). A complete set of buffer factors for acid/base CO2 system in seawater. *Journal of Marine Systems*, *5*(2), 111–118. https://doi.org/10.1016/0924-7963(94)90026-4

Frankignoulle, M., Canon, C., & Gattuso, J. (1994). Marine calcification as a source of carbon dioxide: Positive feedback of increasing atmospheric CO $_2$. *Limnology and Oceanography*, *39*(2), 458–462. https://doi.org/10.4319/lo.1994.39.2.0458

Frankignoulle, M., Pichon, M., & Gattuso, J.-P. (1995). Aquatic Calcification as a Source of Carbon Dioxide. In *Carbon Sequestration in the Biosphere* (pp. 265–271). Springer Berlin Heidelberg. https://doi.org/10.1007/978-3-642-79943-3_18

Friedlingstein, P., O'Sullivan, M., Jones, M. W., Andrew, R. M., Bakker, D. C. E., Hauck, J., Landschützer, P., Le Quéré, C., Li, H., Luijkx, I. T., Peters, G. P., Peters, W., Pongratz, J., Schwingshackl, C., Sitch, S., Canadell, J. G., Ciais, P., Aas, K., Alin, S. R., … Zeng, J. (2025). *Global Carbon Budget 2025*. ESSD – Anthroposphere/Energy and anthropogenic emissions. https://doi.org/10.5194/essd-2025-659

Fuhr, M., Geilert, S., Schmidt, M., Liebetrau, V., Vogt, C., Ledwig, B., & Wallmann, K. (2022). Kinetics of Olivine Weathering in Seawater: An Experimental Study. *Frontiers in Climate*, *4*, 831587. https://doi.org/10.3389/fclim.2022.831587

Fuhr, M., Wallmann, K., Dale, A. W., Diercks, I., Kalapurakkal, H. T., Schmidt, M., Sommer, S., Böhnke, S., Perner, M., & Geilert, S. (2023). Disentangling artificial and natural benthic weathering in organic rich Baltic Sea sediments. *Frontiers in Climate*, *5*, 1245580. https://doi.org/10.3389/fclim.2023.1245580

Fuhr, M., Wallmann, K., Dale, A. W., Kalapurakkal, H. T., Schmidt, M., Sommer, S., Deusner, C., Spiegel, T., Kowalski, J., & Geilert, S. (2024). Alkaline mineral addition to anoxic to hypoxic Baltic Sea sediments as a potentially efficient CO2-removal technique. *Frontiers in Climate*, *6*, 1338556. https://doi.org/10.3389/fclim.2024.1338556

Gasser, T., Guivarch, C., Tachiiri, K., Jones, C. D., & Ciais, P. (2015). Negative emissions physically needed to keep global warming below 2 °C. *Nature Communications*, *6*(1), 7958. https://doi.org/10.1038/ncomms8958

Gattuso, J.-P., Epitalon, J.-M., Lavigne, H., & Orr, J. (2024). *seacarb: Seawater Carbonate Chemistry.* [Computer software]. https://CRAN.R-project.org/package=seacarb

https://doi.org/10.5194/egusphere-2026-2930
Preprint. Discussion started: 1 June 2026

Gazeau, F., Parker, L. M., Comeau, S., Gattuso, J.-P., O'Connor, W. A., Martin, S., Pörtner, H.-O., & Ross, P. M. (2013). Impacts of ocean acidification on marine shelled molluscs. *Marine Biology*, *160*(8), 2207–2245. https://doi.org/10.1007/s00227-013-2219-3

Gazeau, F., Quiblier, C., Jansen, J. M., Gattuso, J., Middelburg, J. J., & Heip, C. H. R. (2007). Impact of elevated CO_2 on shellfish calcification. *Geophysical Research Letters*, *34*(7), 2006GL028554. https://doi.org/10.1029/2006GL028554

Geerts, L. J. J., Hylén, A., & Meysman, F. J. R. (2025). Review and syntheses: Ocean alkalinity enhancement and carbon dioxide removal through marine enhanced rock weathering using olivine. *Biogeosciences*, *22*(2), 355–384. https://doi.org/10.5194/bg-22-355-2025

Glud, R. N. (2008). Oxygen dynamics of marine sediments. *Marine Biology Research*, *4*(4), 243–289. https://doi.org/10.1080/17451000801888726

Goossens, C., Van De Velde, S. J., & Meysman, F. J. R. (2026). A Revised Estimate of Calcium Carbonate Dissolution in Coastal and Shelf Sediments Suggests Large Shelf Exports in the Marine $CaCO_3$ Cycle. *Global Biogeochemical Cycles*, *40*(3), e2025GB008936. https://doi.org/10.1029/2025GB008936

Green, M. A., Jones, M. E., Boudreau, C. L., Moore, R. L., & Westman, B. A. (2004). Dissolution mortality of juvenile bivalves in coastal marine deposits. *Limnology and Oceanography*, *49*(3), 727–734. https://doi.org/10.4319/lo.2004.49.3.0727

Green, M. A., Waldbusser, G. G., Reilly, S. L., Emerson, K., & O'Donnell, S. (2009). Death by dissolution: Sediment saturation state as a mortality factor for juvenile bivalves. *Limnology and Oceanography*, *54*(4), 1037–1047. https://doi.org/10.4319/lo.2009.54.4.1037

Hargrave, B., Doucette, L., Cranford, P., Law, B., & Milligan, T. (2008). Influence of mussel aquaculture on sediment organic enrichment in a nutrient-rich coastal embayment. *Marine Ecology Progress Series*, *365*, 137–149. https://doi.org/10.3354/meps07636

Hu, X., & Cai, W.-J. (2011). An assessment of ocean margin anaerobic processes on oceanic alkalinity budget. *Global Biogeochemical Cycles*, *25*(3), n/a-n/a. https://doi.org/10.1029/2010GB003859

Huettel, M., & Gust, G. (1992). Impact of bioroughness on interfacial solute exchange in permeable sediments. *Marine Ecology Progress Series*, *89*, 253–267. https://doi.org/10.3354/meps089253

Hurvich, C. M., & Tsai, C.-L. (1989). Regression and time series model selection in small samples. *Biometrika*, *76*(2), 297–307. https://doi.org/10.1093/biomet/76.2.297

Hylén, A., & van de Velde, S. (2025). *FLUXER* [Computer software]. Zenodo. https://doi.org/10.5281/zenodo.14758689

IPCC. (2023). *Climate Change 2023: Synthesis Report. Contribution of Working Groups I, II and III to the Sixth Assessment Report of the Intergovernmental Panel on Climate Change [Core Writing Team, H. Lee and J. Romero (eds.)]*. Intergovernmental Panel on Climate Change. https://doi.org/10.59327/IPCC/AR6-9789291691647

Jørgensen, B. B., Wenzhöfer, F., Egger, M., & Glud, R. N. (2022). Sediment oxygen consumption: Role in the global marine carbon cycle. *Earth-Science Reviews*, *228*, 103987. https://doi.org/10.1016/j.earscirev.2022.103987

Keeling, C. D. (1958). The concentration and isotopic abundances of atmospheric carbon dioxide in rural areas. *Geochimica et Cosmochimica Acta*, *13*(4), 322–334. https://doi.org/10.1016/0016-7037(58)90033-4

Keeling, C. D. (1961). The concentration and isotopic abundances of carbon dioxide in rural and marine air. *Geochimica et Cosmochimica Acta*, *24*(3–4), 277–298. https://doi.org/10.1016/0016-7037(61)90023-0

Kleypas, J. A. (2011). Ocean Acidification, Effects on Calcification. In D. Hopley (Ed.), *Encyclopedia of Modern Coral Reefs* (pp. 733–737). Springer Dordrecht. https://doi.org/10.1007/978-90-481-2639-2_118

Lacoste, É., Drouin, A., Weise, A., Archambault, P., & McKindsey, C. (2018). Low benthic impact of an offshore mussel farm in Îles-de-la-Madeleine, eastern Canada. *Aquaculture Environment Interactions*, *10*, 473–485. https://doi.org/10.3354/aei00283

Lan, X., Tans, P., & Thoning, K. W. (2025, July 14). *Trends in globally-averaged CO2 determined from NOAA Global Monitoring Laboratory measurements*. https://doi.org/https://doi.org/10.15138/9N0H-ZH07

Lavoie, M.-F., Lacoste, É., Weise, A. M., & McKindsey, C. W. (2024). Benthic responses to organic enrichment under a mussel (Mytilus edulis) farm. *Frontiers in Marine Science*, *11*, 1433365. https://doi.org/10.3389/fmars.2024.1433365

Lück, S., Callaghan, M., Borchers, M., Cowie, A., Fuss, S., Gidden, M., Hartmann, J., Kammann, C., Keller, D. P., Kraxner, F., Lamb, W. F., Mac Dowell, N., Müller-Hansen, F., Nemet, G. F., Probst, B. S., Renforth, P., Repke, T., Rickels, W., Schulte, I., … Minx, J. C. (2025). Scientific literature on carbon dioxide removal revealed as much larger through

https://doi.org/10.5194/egusphere-2026-2930
Preprint. Discussion started: 1 June 2026

AI-enhanced systematic mapping. *Nature Communications*, *16*(1), 6632. https://doi.org/10.1038/s41467-025-61485-8

Lunstrum, A., & Berelson, W. M. (2022). CaCO3 dissolution in carbonate-poor shelf sands increases with ocean acidification and porewater residence time. *Geochimica et Cosmochimica Acta*, *329*, 168–184. https://doi.org/10.1016/j.gca.2022.04.031

McClintock, J. B., Angus, R. A., Mcdonald, M. R., Amsler, C. D., Catledge, S. A., & Vohra, Y. K. (2009). Rapid dissolution of shells of weakly calcified Antarctic benthic macroorganisms indicates high vulnerability to ocean acidification. *Antarctic Science*, *21*(5), 449–456. https://doi.org/10.1017/S0954102009990198

McKindsey, C. W., Archambault, P., Callier, M. D., & Olivier, F. (2011). Influence of suspended and off-bottom mussel culture on the sea bottom and benthic habitats: A review[1] This review is part of a virtual symposium on current topics in aquaculture of marine fish and shellfish. *Canadian Journal of Zoology*, *89*(7), 622–646. https://doi.org/10.1139/z11-037

Melzner, F., Stange, P., Trübenbach, K., Thomsen, J., Casties, I., Panknin, U., Gorb, S. N., & Gutowska, M. A. (2011). Food Supply and Seawater pCO2 Impact Calcification and Internal Shell Dissolution in the Blue Mussel Mytilus edulis. *PLoS ONE*, *6*(9), e24223. https://doi.org/10.1371/journal.pone.0024223

Meysman, F. J. R., Galaktionov, O. S., Gribsholt, B., & Middelburg, J. J. (2006). Bioirrigation in permeable sediments: Advective pore-water transport induced by burrow ventilation. *Limnology and Oceanography*, *51*(1), 142–156. https://doi.org/10.4319/lo.2006.51.1.0142

Middelburg, J. J., Soetaert, K., & Hagens, M. (2020). Ocean alkalinity, buffering and biogeochemical processes. *Reviews of Geophysics*, *58*. https://doi.org/10.1029/2019RG000681

Minx, J., Burke, J., Schulte, I., Probst, B., Müller-Hansen, F., Roe, S., Buck, H., Smith, S., Injy Johnstone, Nemet, G. F., Edwards, M., Gidden, M., Schenuit, F., Fuss, S., Lamb, W. F., Geden, O., Pongratz, J., Vaughan, N., & Cox, E. (2024). *The State of Carbon Dioxide Removal—2nd Edition*. https://doi.org/10.17605/OSF.IO/F85QJ

Montgomery, D. C., Peck, E. A., & Vining, G. G. (2012). *Introduction to linear regression analysis*. Wiley.

Morse, J. W., & Mackenzie, F. T. (1990). *Geochemistry of sedimentary carbonates*. Elsevier.

Morse, J. W., Zullig, J. J., Bernstein, L. D., Millero, F. J., Milne, P. J., Mucci, A., & Choppin, G. R. (1985). Chemistry of calcium carbonate-rich shallow water sediments in the Bahamas. *American Journal of Science*, *285*(2), 147–185. https://doi.org/10.2475/ajs.285.2.147

Nienhuis, S., Palmer, A. R., & Harley, C. D. G. (2010). Elevated CO_2 affects shell dissolution rate but not calcification rate in a marine snail. *Proceedings of the Royal Society B: Biological Sciences*, *277*(1693), 2553–2558. https://doi.org/10.1098/rspb.2010.0206

Oschlies, A., Bach, L. T., Rickaby, R. E. M., Satterfield, T., Webb, R., & Gattuso, J.-P. (2023). Climate targets, carbon dioxide removal, and the potential role of ocean alkalinity enhancement. *State of the Planet*, *2-oae2023*, 1–9. https://doi.org/10.5194/sp-2-oae2023-1-2023

Pataki, D. E., Ehleringer, J. R., Flanagan, L. B., Yakir, D., Bowling, D. R., Still, C. J., Buchmann, N., Kaplan, J. O., & Berry, J. A. (2003). The application and interpretation of Keeling plots in terrestrial carbon cycle research. *Global Biogeochemical Cycles*, *17*(1). https://doi.org/10.1029/2001GB001850

Pernet, F., Dupont, S., Gattuso, J., Metian, M., & Gazeau, F. (2025). Cracking the myth: Bivalve farming is not a CO $_2$ sink. *Reviews in Aquaculture*, *17*(1). https://doi.org/10.1111/raq.12954

Ray, N. E., O'Meara, T., Wiliamson, T., Izursa, J.-L., & Kangas, P. C. (2018). Consideration of carbon dioxide release during shell production in LCA of bivalves. *The International Journal of Life Cycle Assessment*, *23*(5), 1042–1048. https://doi.org/10.1007/s11367-017-1394-8

Renforth, P., & Henderson, G. (2017). Assessing ocean alkalinity for carbon sequestration. *Reviews of Geophysics*, *55*, 636–674. https://doi.org/10.1002/2016RG000533

Rimstidt, J. D., & Vaughan, D. J. (2003). Pyrite oxidation: A state-of-the-art assessment of the reaction mechanism. *Geochimica et Cosmochimica Acta*, *67*(5), 873–880. https://doi.org/10.1016/S0016-7037(02)01165-1

Sanderson, B. M., O'Neill, B. C., & Tebaldi, C. (2016). What would it take to achieve the Paris temperature targets? *Geophysical Research Letters*, *43*(13), 7133–7142. https://doi.org/10.1002/2016GL069563

Smith, S. V., & Mackenzie, F. T. (2016). The role of CaCO3 reactions in the contemporary oceanic CO2 cycle. *Aquatic Geochemistry*, *22*, 153–175. https://doi.org/10.1007/s10498-015-9282-y

https://doi.org/10.5194/egusphere-2026-2930
Preprint. Discussion started: 1 June 2026

Soetaert, K., Hofmann, A. F., Middelburg, J. J., Meysman, F. J. R., & Greenwood, J. (2007). The effect of biogeochemical processes on pH. *Marine Chemistry*, *105*(1–2), 30–51. https://doi.org/10.1016/j.marchem.2006.12.012

Subhas, A. V., Dong, S., Naviaux, J. D., Rollins, N. E., Ziveri, P., Gray, W., Rae, J. W. B., Liu, X., Byrne, R. H., Chen, S., Moore, C., Martell-Bonet, L., Steiner, Z., Antler, G., Hu, H., Lunstrum, A., Hou, Y., Kemnitz, N., Stutsman, J., … Adkins, J. F. (2022). Shallow Calcium Carbonate Cycling in the North Pacific Ocean. *Global Biogeochemical Cycles*, *36*(5). https://doi.org/10.1029/2022GB007388

Thrane, M. (2004). Energy Consumption in the Danish Fishery: Identification of Key Factors. *Journal of Industrial Ecology*, *8*(1–2), 223–239. https://doi.org/10.1162/1088198041269427

Waldbusser, G. G., Steenson, R. A., & Green, M. A. (2011). Oyster Shell Dissolution Rates in Estuarine Waters: Effects of pH and Shell Legacy. *Journal of Shellfish Research*, *30*(3), 659–669. https://doi.org/10.2983/035.030.0308

Welladsen, H. M., Southgate, P. C., & Heimann, K. (2010). The effects of exposure to near-future levels of ocean acidification on shell characteristics of Pinctada fucata (Bivalvia: Pteriidae). *Molluscan Research*, *30*(3). https://doi.org/10.11646/mr.30.3.2

Wilson, P. S., & Vopel, K. (2015). Assessing the Sulfide Footprint of Mussel Farms with Sediment Profile Imagery: A New Zealand Trial. *PLOS ONE*, *10*(6), e0129894. https://doi.org/10.1371/journal.pone.0129894

Zeebe, R. E., & Wolf-Gladrow, D. (2001). *CO2 in seawater: Equilibrium, kinetics, isotopes*.